Solid State Sciences 52 (2016) 97–105

Contents lists available at ScienceDirect

Solid State Sciences

journal homepage: www.elsevier.com/locate/ssscie

Intense turquoise colors of apatite-type compounds with Mn^{5+} in tetrahedral coordination

Elena A. Medina [a], Jun Li [a, *], Judith K. Stalick [b], M.A. Subramanian [a]

[a] Department of Chemistry, Oregon State University, Corvallis, OR 97331, United States
[b] NIST Center for Neutron Research, National Institute of Standards and Technology, 100 Bureau Drive, Gaithersburg, MD 20899, United States

ARTICLE INFO

Article history:
Received 4 October 2015
Received in revised form
22 November 2015
Accepted 1 December 2015
Available online 11 December 2015

Keywords:
Inorganic pigments
Apatite-type structure
Synthesis
Neutron diffraction
Optical properties
Magnetism

ABSTRACT

The solid solutions of chlorapatite compounds $Ba_5Mn_{3-x}V_xO_{12}Cl$ ($x = 0$–3.0) and $Ba_5Mn_{3-x}P_xO_{12}Cl$ ($x = 0$–3.0) have been synthesized through solid state reactions and Pechini or sol–gel method using citric acid. The colors of the samples change from white ($x = 3.0$) through turquoise ($x = 1.5$) to dark green ($x = 0$) with increasing amount of manganese. Optical measurements reveal that the origin of the color is presumably a combination of d–d transitions of Mn^{5+} and cation-anion charge transfer from transition metals to oxygens. Near IR reflectance measurements indicate that synthesized compounds are promising materials for "cool pigments" applications. Magnetic measurements verify that manganese has two unpaired electrons and exhibits 5 + oxidation state. The IR spectra change systematically with sample compositions and the fingerprint region (700 cm^{-1} to 1100 cm^{-1}) indicates characteristic bands belonging to $(MnO_4)^{3-}$, $(VO_4)^{3-}$ and $(PO_4)^{3-}$ functional groups. Structure refinements using neutron data confirm that Mn^{5+}, V^{5+} and P^{5+} cations occupy the tetrahedral sites in the apatite structure.

1. Introduction

The search for new, cheap, enduring and environmentally friendly inorganic pigments is a challenging task of materials science. It was discovered recently that hexagonal $YIn_{1-x}Mn_xO_3$ solid solution with Mn^{3+} in trigonal bipyramidal coordination gives a brilliant blue color and exhibits excellent near-infrared reflectance [1]. The new blue pigments are easy to make, heat- and acid-resistant and nontoxic with great potential for cool pigment applications where heating is not desirable (e.g., roofing materials). The cost of indium-based pigments however is an obstacle for practical applications. New inexpensive blue pigments with similar optical properties are needed.

Many Mn-containing compounds have been reported with vivid colors. Brownmillerite-type $Ba_2In_{2-x}Mn_xO_{5+x}$ produces a green color with Mn^{5+} in tetrahedral coordination [2]. A minimum in the visible absorption at 500 nm is responsible for the color of these compounds. The Apatite-type structure $A_5(MO_4)_3X$ (A – Ca^{2+}, Sr^{2+}, Ba^{2+}, Pb^{2+}; M – P^{5+}, Mn^{5+}, Cr^{5+}, V^{5+}; X – F^-, Cl^-, OH^-) [3–12] gives a great possibility to combine different A, M and X – site elements and synthesize compounds with a wide range of useful properties. A great number of compounds with the Apatite related structure occur in nature and form minerals belonging to the apatite ($A^{II}{}_5(M^VO_4)_3X$), belovite ($A^{II}B^{II}C^{II}{}_3(M^VO_4)_3X$), britholite ($(A^{III},B^{II})_5(M^{IV}O_4)_3X$) [13,14], hedyphane ($A^{II}{}_2B^{II}{}_3(M^VO_4)_3X$) and ellestadite ($A^{II}{}_5(M_1^{IV}O_4)_{1.5}(M_2^{VI}O_4)_{1.5}X$) mineral groups [15]. Apatite-type compounds containing Mn^{5+} tetrahedrally coordinated by oxygen might be promising materials for pigments with deep blue and green colors [16,17]. In inorganic oxides the oxidation state 5 + of manganese is very unusual, because Mn^{5+} is unstable and has a tendency to disproportionate into more stable oxidation states 4 + and 7+. Apatite-type compounds with Mn^{5+} in tetrahedral coordination (M – site cation) exist mostly with Ba^{2+} as an A – site cation, which due to its high ($\approx$5eV) first ionization potential helps manganese to keep the unusual oxidation state [18]. Several solid solutions with the apatite host structure have been synthesized and colors of compounds were described [19,20], but no detailed and systematic structural, optical and magnetic data are reported.

The parent compound $Ba_5(MnO_4)_3Cl$ crystallizes in space group $P6_3/m$ ($a = 10.48$ Å, $c = 7.772$ Å, $V = 739.4$ Å^3) [21–24], isostructural with $Ba_5(VO_4)_3Cl$ [25–28] and $Ba_5(PO_4)_3Cl$ [29–43] (Fig. 1). There are two crystallographic sites of Ba^{2+} in the hexagonal structure (4f and 6h) differing in coordination number and local symmetry. The Ba1 atoms occupying 4f positions have a coordination number of 9,

* Corresponding author. Department of Chemistry, Oregon State University, Gilbert 153, Corvallis, OR 97331, United States.
E-mail address: liju@science.oregonstate.edu (J. Li).

http://dx.doi.org/10.1016/j.solidstatesciences.2015.12.001
1293-2558/

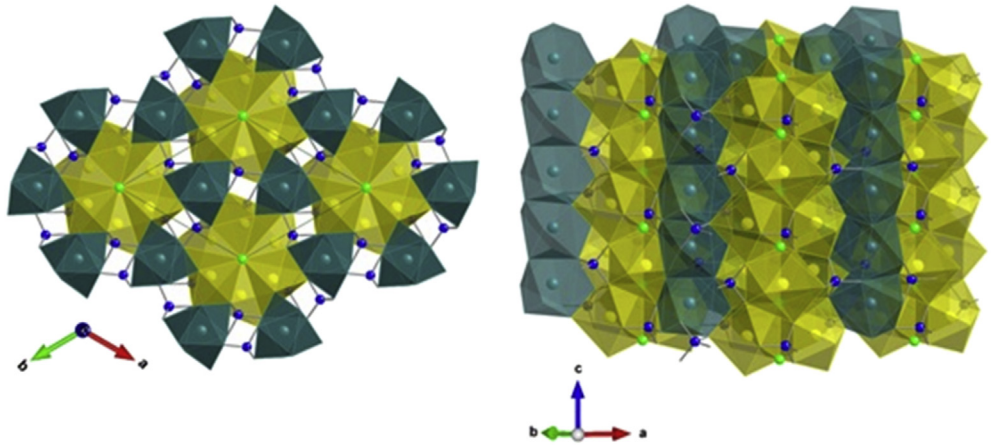

Fig. 1. Hexagonal unit cell of $Ba_5(MnO_4)_3Cl$ structure (left and right): Dark turquoise and yellow spheres represent two different crystallographic positions of Ba^{2+} 4f (Ba1) and 6h (Ba2) accordingly, with face-sharing Ba(1)O9 and edge-sharing Ba(2)O6Cl2 polyhedra forming one-dimensional chains arranged alternately along the c axis. The Mn (blue) tetrahedra are corner-shared with Ba polyhedra and the Cl (green) atoms are lined up in channels along the c axis. Oxygen atoms are omitted for clarity. (For interpretation of the references to color in this figure legend, the reader is referred to the web version of this article.)

forming face-sharing $Ba(1)O_9$ tricapped trigonal prism chains along the c axis. The Ba2 atoms occupying 6h positions are bonded to six oxygens and two chlorines, forming edge-sharing $Ba(2)O_6Cl_2$ bicapped trigonal prism (distorted) chains in channels of $Ba(1)O_9$ chains. The discrete MnO_4 tetrahedra interconnect the one-dimensional Ba polyhedral chains to form the three-dimensional crystal structure. Chlorine atoms are located between layers formed by MnO_4 tetrahedra and stacked up in channels of Ba polyhedral chains along the c axis. For further structural descriptions of the apatite framework see Fig. S1 in supporting information (SI).

In the present work two apatite-type solid solutions, $Ba_5Mn_{3-x}V_xO_{12}Cl$ and $Ba_5Mn_{3-x}P_xO_{12}Cl$, were successfully synthesized and their structural, optical and magnetic properties were studied in detail using various experimental methods and techniques. The end members of the solid solutions are dark green ($Ba_5(MnO_4)_3Cl$) and white ($Ba_5(PO_4)_3Cl$ and $Ba_5(VO_4)_3Cl$), while the colors of the solid solutions vary from dark green to bright turquoise with different shades when Mn^{5+} cations are gradually substituted by isovalent V^{5+} and P^{5+}. Several minerals and pigments with turquoise color are well-known and used today (amazonite, vivianite, blue zircon, chalcedony, some types of spinel and beryl). The most famous among them is the opaque gem called turquoise with the formula $CuAl_6(PO_4)_4(OH)_8 \bullet 4H_2O$ [44]. Some widely used commercial turquoise pigments contain toxic cobalt and chromium [45–47]. The apatite-related pigments described here are more environmentally friendly and thermally stable with brighter colors.

2. Experimental section

All samples were synthesized using standard solid state synthesis. Stoichiometric amounts of $BaCO_3$ (Cerac, 99.9%), MnO_2 (Alfa Aesar, 99.9%), V_2O_5 (Cerac, 99.9%), $BaCl_2 \bullet 2H_2O$ (Mallinckrodt, 99.9%) and $(NH_4)_2HPO_4$ (Mallinckrodt, 99.9%) were ground in an agate mortar, pelletized and heated in an alumina crucible at 800 °C for 12 h in air. The mixture was then ground again, pelletized and reheated at 850 °C for 12 h.

Low temperature synthesis (sol–gel method) was also attempted for the $Ba_5Mn_{3-x}V_xO_{12}Cl$ system. Stoichiometric amounts of $Ba(NO_3)_2$ (Mallinckrodt, 99.9%), $Mn(NO_3)_2 \bullet 4H_2O$ (Aldrich, 99.99%), NH_4Cl (Macron, 99.9%) were mixed and dissolved in DI water. The nitrate solutions were heated while stirring, and the citric acid (Sigma–Aldrich, ≥ 99.5%) was added in a molar ratio of 2:1 citric acid to metal nitrates. Here the citric acid is used as a cross linking agent. The pH of the resulting solutions was then adjusted to 7 using aqueous NH_4OH (28–30% solution, ACS), and the neutralized solutions were heated until the formation of dry gel. Dark brown amorphous powder was obtained after heating the translucent dry gel at 250 °C for 2 h, and it was further calcined at 700–750 °C in air for 12 h.

XRD data were collected using a Rigaku MiniFlex II diffractometer with CuKα radiation (λ = 1.5418 Å) and a graphite monochromator at room temperature. For phase identification the measurements were carried out at 0.5°/min within 15°–70° 2θ range. For lattice parameter calculation the data were collected with an internal standard such as Si. Powder neutron diffraction data were collected on the 32-counter high-resolution diffractometer BT-1 at the Center for Neutron Research at the National Institute of Standards and Technology. A Cu(311) monochromator, yielding a wavelength of 1.5403(2) Å, was employed. Collimation of 15′ of arc was used before the monochromator, 20′ before the sample, and 7′ before the detectors. The samples were loaded into vanadium containers of 15.6 mm diameter and 50 mm length. Data were collected at room temperature over a 2θ range of 3°–167°. XRD and neutron data were refined using the Rietveld method, as implemented in GSAS-EXPGUI software [48,49]. Bond-valence analysis of the neutron structures made use of the bond-valence calculator [50].

Konica Minolta CM-700d Spectrophotometer (Standard illuminant D_{65}) was used to measure L*, a*, b* color coordinates. Diffuse reflectance data in the visible range were measured using a homemade UV-VIS spectrophotometer (MgO as the reference) and converted to absorbance using the Kubelka-Munk equation [51]. Near-infrared reflectance data (up to 2500 nm) were collected using a Jasco V-670 Spectrophotometer. IR measurements were performed using a Thermo Scientific Nicolet 6700 FT-IR Spectrometer in the spectral range of 700 cm^{-1} to 2500 cm^{-1}.

Magnetic properties measurements were made using a Quantum Design Physical Property Measurement System (QD-PPMS) at temperature range of 5 K–300 K (zero-field cooling, applied magnetic field 0.5 T). Inverse magnetic susceptibility data was used to

fit for Curie–Weiss law. Diamagnetic corrections were made for calculations of experimental μ_B [52].

3. Results and discussion

3.1. Crystal structures by X-ray and neutron diffraction

The XRD patterns are similar for $Ba_5Mn_{3-x}V_xO_{12}Cl$ and $Ba_5Mn_{3-x}P_xO_{12}Cl$ samples prepared by solid state reaction and sol–gel method. Diffraction data on samples from solid state reactions were used for structural analysis, as shown in Fig. 2. Nearly all the samples are pure with two exceptions: $Ba_5(PO_4)_3Cl$ has two visible small impurity peaks belong to $Ba(PO_3)_2$ and $Ba_5(VO_4)_3Cl$ contains a small amount of $Ba_2V_2O_7$ impurity phase. With increasing substitution of manganese with vanadium in the structure there are no visible peak shifts because the ionic radii of *M*-site cations differ only slightly.

Based on structure refinements all members of both series are isostructural, with the same hexagonal unit cell ($P6_3/m$) as the parent compounds or end-members of the series. The unit cell (*a*, *c*, cell volume *V*, and *c/a* ratio) variations with *x* (vanadium/phosphorus content) are shown in Fig. 3. There is a gradual increase of the *a* cell parameter and *V* in the case of $Ba_5Mn_{3-x}V_xO_{12}Cl$ solid solution with substitution of smaller cations Mn^{5+} (0.33 Å) by larger cations V^{5+} (0.355 Å) [53]. Cell edge *c*, however, decreases slightly with increasing vanadium substitution. There is a slight deviation from Vegard's law in the case of $Ba_5Mn_{3-x}P_xO_{12}Cl$ solid solution; unit cell edges *a*, *c* and cell volume *V* progressively decrease with increasing P^{5+} (0.17 Å) content. The unit cell parameter *c* decreases with increasing *x* value for both solid solutions. Generally, the *a* parameter changes faster than *c* with *x* or an increase/decrease in the size of *M* has a more pronounced impact on the *a* cell edge. This phenomenon is a consequence of the fact that the apatite structure is more amenable to expansion/compression in the direction of the *a* axis due to the difference in connection of barium polyhedra along the *a* and *c* axes – along the *c* axis the structure is more rigid. The *c/a* ratio varies strongly because of the difference in average V–O/P–O and Mn–O bond lengths. All experimentally obtained unit cell parameters are in a good agreement with the literature data.

Neutron diffraction data on $Ba_5Mn_{3-x}V_xO_{12}Cl$ (x = 0, 0.5, 2.8) and $Ba_5Mn_{0.5}P_{2.5}O_{12}Cl$ samples were collected and the crystal structures were refined using the Rietveld fitting method. The observed and calculated diffraction patterns for $Ba_5Mn_{0.2}V_{2.8}O_{12}Cl$ are shown in Fig. 4 and those for $Ba_5(MnO_4)_3Cl$, $Ba_5Mn_{2.5}V_{0.5}O_{12}Cl$ and $Ba_5Mn_{0.5}P_{2.5}O_{12}Cl$ can be found in Supporting Information (Fig. S2–S4). The structural refinement results are shown in Tables 1–5, and bond valence sums (BVS) were calculated using the bond-valence calculator. Refined anisotropic *U* values are available in CIF files in the Supporting Information.

The refinement of atomic site occupancies shows that there are no oxygen or chlorine vacancies in the structures, i.e. oxygen and chlorine sites are fully occupied. Occupancies of vanadium atoms in the compounds were not refined because vanadium doesn't scatter neutrons much; all vanadium occupancies shown in the tables were calculated based on refined manganese occupancies. Refined atomic displacement parameter *U* values are reasonable and calculated bond valence sums are as expected. Mn^{5+}, V^{5+}, P^{5+} occupy the same crystallographic sites in the structure and have tetrahedral coordination, bonded to four oxygen atoms.

Bond distances and angles for $Ba_5Mn_{0.2}V_{2.8}O_{12}Cl$ are shown in Table 6 and those for $Ba_5(MnO_4)_3Cl$, $Ba_5Mn_{2.5}V_{0.5}O_{12}Cl$, and $Ba_5Mn_{0.5}P_{2.5}O_{12}Cl$ are given in supporting information (Tables S1–S3). The *M*-O bonds in $(MO_4)^{3-}$ tetrahedra become shorter and more covalent with increasing of Mn content in the case of $Ba_5Mn_{3-x}V_xO_{12}Cl$ solid solution (average *M*-O bond length of $Ba_5(MnO_4)_3Cl$ equals 1.699(5) Å and 1.711(8) Å for $Ba_5Mn_{0.2}V_{2.8}O_{12}Cl$).

The main differences in the studied structures occur in the tetrahedrally coordinated *M*-atoms (Fig. 5). A change of the tetrahedral central atom leads to modifications of polyhedra parameters (bond lengths and bond angles). To describe the distortion of tetrahedra the bond angle variance (BAV) and bond length distortion (BLD) parameters might be used [54,55]. BAV and BLD are used to characterize any polyhedra deviations from the ideal geometry. The bond angle variance (BAV) can be calculated using $\sum_{i=1}^{n}(\theta_i-\theta_o)^2/n-1$ equation (θ_o = ideal bond angle for a regular polyhedron, n = number of bond angles in polyhedron and θ_i = individual bond angles). BLD = $100/n\sum_{i=1}^{n}\left|((M\text{-}X)_i\text{-}(M\text{-}X)_m/(M\text{-}X)_m\right|$($i$ = individual bond lengths, m = average bond length and n = number of bonds). These parameters were calculated for $Ba_5Mn_{0.2}V_{2.8}O_{12}Cl$, $Ba_5(MnO_4)_3Cl$ and $Ba_5Mn_{0.5}P_{2.5}O_{12}Cl$ phases based on our Rietveld refinement and compared with the same parameters for $Ba_5(VO_4)_3Cl$ and $Ba_5(PO_4)_3Cl$ compounds, which were calculated based on the literature data. The average bond angles O-*M*-O in $(MO_4)^{3-}$ tetrahedra slightly varies for both series with increasing *x* value (V/P content). The mean O-*M*-O angle equals 108.72°, 109.40°, 109.45°, 109.48° and 109.47° for

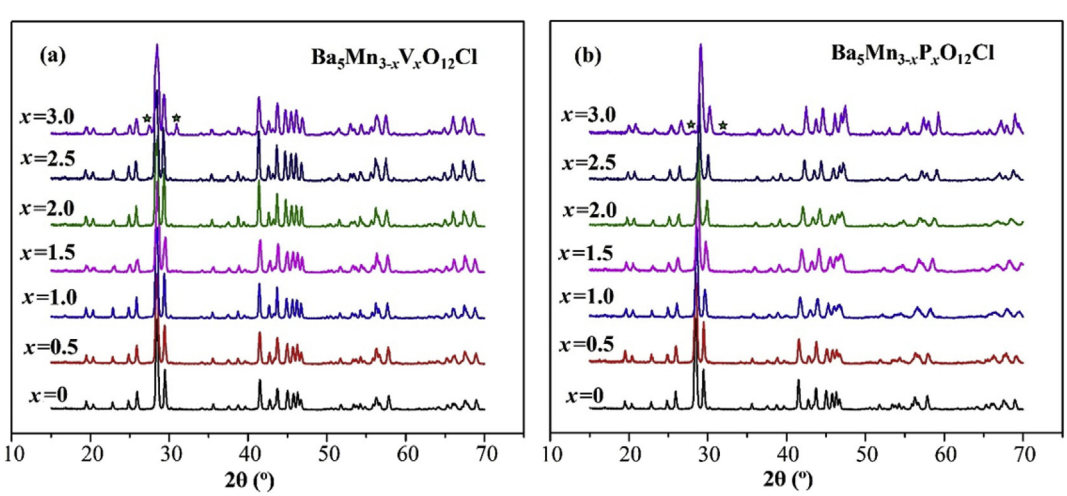

Fig. 2. XRD patterns of $Ba_5Mn_{3-x}V_xO_{12}Cl$ (a) and $Ba_5Mn_{3-x}P_xO12Cl$ (b) samples (asterisk – impurity peaks).

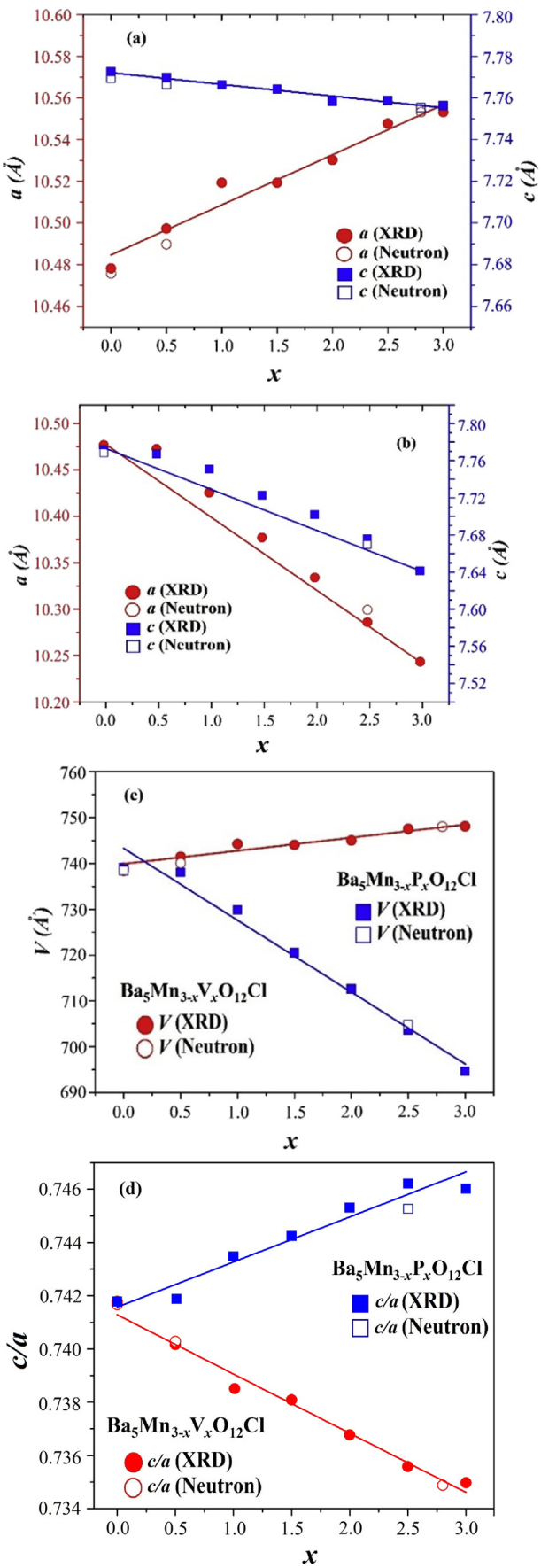

Fig. 3. Unit cell edges of $Ba_5Mn_{3-x}V_xO_{12}Cl$ (a) and $Ba_5Mn_{3-x}P_xO12Cl$ (b) phases, cell volumes (c) and *c*/*a* ratio showing anisotropic structural change (d) of both solid solutions as a function of *x* (vanadium/phosphorus content). The estimated errors for *a*, *c*, and *V* are less than the size of the points in the figures.

$Ba_5(VO_4)_3Cl$, $Ba_5Mn_{0.2}V_{2.8}O_{12}Cl$, $Ba_5(MnO_4)_3Cl$, $Ba_5Mn_{0.5}P_{2.5}O_{12}Cl$ and $Ba_5(PO_4)_3Cl$, respectively (ideal tetrahedral angle is 109.47°). The O-*M*-O bond angle for the larger $(VO_4)^{3-}$ tetrahedra deviate more from 109.47°; this fact is confirmed by BAV values (BAV($Ba_5(VO_4)_3Cl$) = 13.7, BAV($Ba_5Mn_{0.2}V_{2.8}O_{12}Cl$) = 13.5, BAV($Ba_5(MnO_4)_3Cl$) = 12.8, BAV($Ba_5Mn_{0.5}P_{2.5}O_{12}Cl$) = 2.93 and BAV($Ba_5(PO_4)_3Cl$) = 2.35. There is an opposite trend in the case of BLD values; with decreasing of M^{5+} ionic radius BLD increases. The smaller tetrahedral $(PO_4)^{3-}$ anion is more distorted, where $Ba_5(PO_4)_3Cl$ has the highest value of BLD = 0.83 BLD($Ba_5(VO_4)_3Cl$) = 0.19, BLD($Ba_5Mn_{0.2}V_{2.8}O_{12}Cl$) = 0.21, BLD($Ba_5(MnO_4)_3Cl$) = 0.39 and BLD($Ba_5Mn_{0.5}P_{2.5}O_{12}Cl$) = 0.82).

3.2. Optical properties

Optical properties were characterized to study the evolution of colors of the solid solutions and understand structure-property relationships. The substituted samples have very bright colors, varying from light to dark turquoise and dark green (Mn-rich ends of solid solutions); the end members $Ba_5(PO_4)_3Cl$ and $Ba_5(VO_4)_3Cl$ have a white color (Fig. 6). To characterize the color of $Ba_5Mn_{3-x}M_xO_{12}Cl$ (*M* = V, P) samples, the L*, a*, b* color coordinates were measured [56] (L*a*b* color sphere and YXY color space for both series are given in Fig. S5–S8). As shown in Fig. 7, the L* and a* values gradually increase with increasing of *x* value, while the b* values decrease as *x* moves to the vanadium/phosphorous-rich sides of the solid solutions.

Interatomic excitations (*d*–*d* transitions) in Mn^{5+} (tetrahedral coordination) are mainly responsible for the color of the samples. There are two transitions that significantly impact the visible spectrum and thus color. The ground state e_2 has two states with two unpaired electrons. There are just two fully allowed transitions to examine: one electron up to t_2 ($e^1t^1{}_2$) and two electrons up to t_2 ($e^0t^2{}_2$). The one-electron transition gives the blue color. The two-electron transition has a higher energy and lower probability. Consequently, the second transition is what changes blue to blue-green (turquoise) color. It is possible that this less probable two-electron transition is intensified by the high oxidation state (5+) of the manganese ion and this is the reason it is most enhanced for barium containing compounds where Mn–O covalency is very high.

Diffuse reflectance spectra of the $Ba_5Mn_{3-x}V_xO_{12}Cl$ series are shown in Fig. 8. All $Ba_5Mn_{3-x}V_xO_{12}Cl$ ($x = 0$–2.9) samples show two maximum peaks in the red-orange (≈630 nm) and purple (≈380 nm) regions and one minimum in the green-blue region (≈500 nm–520 nm); this combination causes the green or turquoise color of the compounds. $Ba_5V_3O_{12}Cl$ and $Ba_5P_3O_{12}Cl$ don't absorb in the visible region and the color of these samples is white. On each absorbance vs. wavelength spectrum there are two shoulders, which are present in the high- and low-energy regions of the visible spectrum. The low-energy peak is due to the allowed transitions of electrons (*d*–*d* transitions) inside the manganese atom and the high-energy peak is due to a Mn^{5+}-O^{2-} charge transfer transition. The intensity of the samples' absorbance goes down with decreasing of manganese content (*x* increases), because the *d*–*d* transition's contribution becomes smaller, and the samples become lighter. At the same time the minimum of absorbance becomes broader, though it still exists in the spectrum of the lightest sample (*x* = 2.5) and completely disappears for white samples

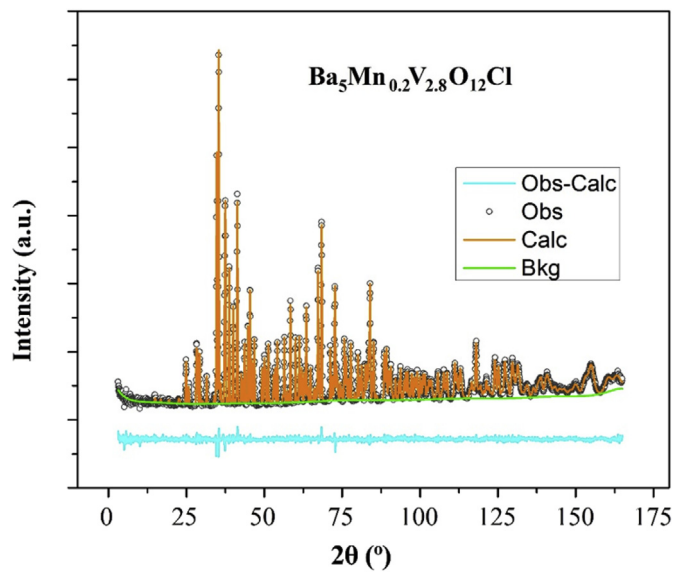

Fig. 4. Neutron data of $Ba_5Mn_{0.2}V_{2.8}O_{12}Cl$ phase shown with a Rietveld fit.

Table 1
Cell parameters by Rietveld refinement of $Ba_5Mn_{3-x}M_xO_{12}Cl$ (M = V, P).

Composition	$x = 0$	M = V, $x = 0.5$	M = V, $x = 2.8$	M = P, $x = 2.5$
a (Å)	10.482(5)	10.490(7)	10.553(2)	10.301(0)
c (Å)	7.7744(7)	7.7660(7)	7.7553(5)	7.6702(4)
V (Å^3)	739.82(4)	740.19(1)	748.00(2)	704.85(3)
R_{wp} (%)	4.67	4.64	4.41	5.75
χ^2	1.08	1.12	1.00	2.99

shifts toward longer wavelength with increasing manganese content as the sample color goes from turquoise to dark green. With decreasing amount of vanadium/phosphorus (when x value decreases) metal-oxygen M-O bonds become more covalent and the crystal field around the M-atom changes resulting in the peak shifting. The $(MnO_4)^{3-}$ group shows five reflectance peaks and absorbance valleys in the 400 nm–1400 nm region, which are related to five interatomic transitions of the Mn^{5+} cation [57–60]. All synthesized samples show these transitions in the studied region: $e^2\,(^3A_2) \rightarrow t_2^2\,(^3T_1 = {}^3P)$ (≈300 nm); $e^2\,(^3A_2) \rightarrow e^1t_2^1\,(^3T_1 = {}^3F)$ (≈700 nm) and $e^2\,(^3A_2) \rightarrow e^1t_2^1\,(^3T_2)$ (≈900 nm) are spin allowed transitions and two are spin forbidden: $e^2\,(^3A_2) \rightarrow e^2\,(^1A_1)$ (≈800 nm) and there is minimum peak around 1200 nm, which corresponds to $e^2\,(^3A_2) \rightarrow e^2\,(^1E)$ transition. Intensity of reflectance goes down from light turquoise to dark-green samples. The abrupt change in the IR reflectance of $Ba_5Mn_{3-x}V_xO_{12}Cl$ solid solution near 800 nm is probably due to the effect of fluorescence in samples containing manganese and vanadium together; samples with $x = 0$ and $x = 3$ do not show this phenomenon. The reflectance of the samples in the 750 nm–2500 nm region where "cool pigments" display high reflectance is around 70%–85%. All synthesized compounds are promising materials for "cool pigments" applications.

3.3. IR investigation

Based on literature data the most intense vibrational modes in apatite-type compounds are due to vibrations of $(MO_4)^{3-}$ tetrahedra; the group has characteristic bands in the 700 cm^{-1} to 1100 cm^{-1} IR region [61–63]. Positions and shapes of vibrational peaks depend on symmetry of the group, distortion of atoms from ideal tetrahedral coordination and origin of atoms surrounding M

Table 2
Neutron structural refinement of $Ba_5(MnO_4)_3Cl$. The chemical formula of compound based on the refined occupancies is $Ba_5(MnO_4)_3Cl$.

Atoms	Wyckoff position	BVS	x	y	z	Occupancy	U_{iso} (Å^2)
Ba1	4f	2.1	1/3	2/3	0	1.00	0.009(4)
Ba2	6h	1.9	0.2585(8)	0.0132(1)	1/4	1.00	0.009(3)
Mn1	6h	4.7	0.3706(6)	0.4046(5)	1/4	1.00	0.009(4)
Cl1	2b	1.2	0	0	0	1.00	0.012(8)
O1	6h	1.9	0.4798(0)	0.3267(8)	1/4	1.00	0.016(6)
O2	6h	2.1	0.4688(9)	0.5925(8)	1/4	1.00	0.009(0)
O3	12i	1.9	0.2589(7)	0.3543(5)	0.0757(7)	1.00	0.014(1)

Table 3
Neutron structural refinement of $Ba_5Mn_{2.5}V_{0.5}O_{12}Cl$. The chemical formula of compound based on the refined occupancies is $Ba_5Mn_{2.6}V_{0.4}O_{12}Cl$.

Atoms	Wyckoff position	BVS	x	y	z	Occupancy	U_{iso} (Å^2)
Ba1	4f	2.1	1/3	2/3	0	1.00	0.008(8)
Ba2	6h	1.9	0.2576(6)	0.0120(6)	1/4	1.00	0.012(3)
Mn1	6h	5.0	0.3717(2)	0.4051(2)	1/4	0.85(2)	0.008(0)
V1	6h	5.0	0.3717(2)	0.4051(2)	1/4	0.15	0.006(8)
Cl1	2b	1.0	0	0	0	1.00	0.011(3)
O1	6h	1.9	0.4796(9)	0.3272(4)	1/4	1.00	0.019(2)
O2	6h	2.1	0.4693(8)	0.5920(1)	1/4	1.00	0.011(2)
O3	12i	1.8	0.2586(6)	0.3545(4)	0.0760(4)	1.00	0.000(3)

($x = 3$), which do not absorb in the visible region.

Near-Infrared reflectance spectra were measured to examine the potential cool pigment application of the samples (Fig. S9, S10). UV–vis and NIR reflectance of $Ba_5Mn_{3-x}V_xO_{12}Cl$ ($x = 0, 2.5, 3$) and $Ba_5Mn_{3-x}P_xO_{12}Cl$ ($x = 0, 2.5, 3$) samples as a function of wavelength are shown in Fig. 9. There is one peak around 500 nm in the visible region for the colored samples, and the maximum of this peak

cation. IR spectra of $Ba_5Mn_3O_{12}Cl$, $Ba_5Mn_{2.5}V_{0.5}O_{12}Cl$, $Ba_5Mn_{0.2}V_{2.8}O_{12}Cl$ and $Ba_5Mn_{0.5}P_{2.5}O_{12}Cl$ phases were obtained. Measured spectra of the compounds, all vibrations and their wavenumbers for these phases are given in the Supporting Information (Fig. S11 And Table S4). Vibrations with higher wavenumbers (300 cm^{-1} to 900 cm^{-1}) belong to deformation vibrations (ν_1 – symmetrical and ν_3 – asymmetrical) of $(VO_4)^{3-}$ group; modes with smaller

Table 4
Neutron structural refinement of $Ba_5Mn_{0.2}V_{2.8}O_{12}Cl$. The chemical formula of compound based on the refined occupancies is $Ba_5Mn_{0.3}V_{2.7}O_{12}Cl$.

Atoms	Wyckoff position	BVS	*x*	*y*	*z*	Occupancy	U_{iso} (Å^2)
Ba1	4f	2.1	1/3	2/3	0	1.00	0.011(1)
Ba2	6h	1.8	0.2455(1)	0.9884(7)	1/4	1.00	0.006(2)
V1	6h	5.1	0.4055(1)	0.3717(2)	1/4	0.90	0.010(2)
Mn1	6h	5.1	0.4055(1)	0.3717(2)	1/4	0.10(1)	0.007(1)
Cl1	2b	1.0	0	0	0	1.00	0.013(1)
O1	6h	1.8	0.3267(0)	0.4802(1)	1/4	1.00	0.018(8)
O2	6h	2.1	0.5926(5)	0.4694(9)	1/4	1.00	0.007(0)
O3	12i	1.8	0.3540(3)	0.2590(5)	0.0743(1)	1.00	0.020(9)

Table 5
Neutron structural refinement of $Ba_5Mn_{0.5}P_{2.5}O_{12}Cl$. The chemical formula of compound based on the refined occupancies is $Ba_5Mn_{0.5}P_{2.5}O_{12}Cl$.

Atoms	Wyckoff position	BVS	*x*	*y*	*z*	Occupancy	U_{iso} (Å^2)
Ba1	4f	2.1	1/3	2/3	0	1.00	0.010(3)
Ba2	6h	1.8	0.2453(4)	0.2592(4)	1/4	1.00	0.013(9)
P1	6h	4.7	0.4049(7)	0.0350(2)	1/4	0.84(9)	0.007(0)
Mn1	6h	4.7	0.4049(7)	0.0350(2)	1/4	0.15(1)	0.031(6)
Cl1	2b	1.0	0	0	0	1.00	0.008(9)
O1	6h	1.9	0.3397(1)	−0.1388(7)	1/4	1.00	0.024(3)
O2	6h	2.1	0.5821(7)	0.1189(5)	1/4	1.00	0.010(6)
O3	12i	1.9	0.3547(5)	0.0855(4)	0.0855(9)	1.00	0.021(7)

Table 6
Selected geometric parameters: bond lengths (Å) and angles (°) of $Ba_5Mn_{0.2}V_{2.8}O_{12}Cl$.

Ba1–O1 x3	2.737(2)	Ba2–O1	2.962(4)
Ba1–O2 x3	2.749(8)	Ba2–O2	2.606(0)
Ba1–O3 x3	3.040(9)	Ba2–O3 x2	2.692(1)
Mn1/V1–O3 x2	1.708(6)	Ba2–O3 x2	2.837(5)
Mn1/V1–O2	1.710(9)	Ba2–Cl1 x2	3.286(6)
Mn1/V1–O1	1.718(9)		
O1–Mn1/V1–O3	111.8(4)	Cl1–Ba2–Cl1	72.30(1)
Ba1–O3–Mn1/V1	92.61(5)	O2–Mn1/V1–O3	106.8(0)
Ba2–O1–Mn1/V1	101.2(6)		

wavenumbers (1000 cm^{-1} to 1200 cm^{-1}), because the P–O bond is shorter than V–O and Mn–O bonds. All vibrations located below these regions are vibrations of the lattice, and vibrations lying above are composite vibrations. Due to the large mass of the chlorine atom, its vibrations cannot be detected in the measured region; they are shifted towards the smaller wavenumbers and lie below 200 cm^{-1}. The $Ba_5Mn_{0.5}P_{2.5}O_{12}Cl$ sample shows three $(PO_4)^{3-}$ group vibrational modes around 1000 cm^{-1} (fingerprint region of the group), which correspond to ν_1 and ν_3 modes. All samples have the ν_3 vibrational peak of $(MnO_4)^{3-}$ around 730 cm^{-1} to 770 cm^{-1}. Vanadium containing samples $Ba_5Mn_{2.5}V_{0.5}O_{12}Cl$ and $Ba_5Mn_{0.2}V_{2.8}O_{12}Cl$ show the ν_3 vibrational mode of $(VO_4)^{3-}$ group

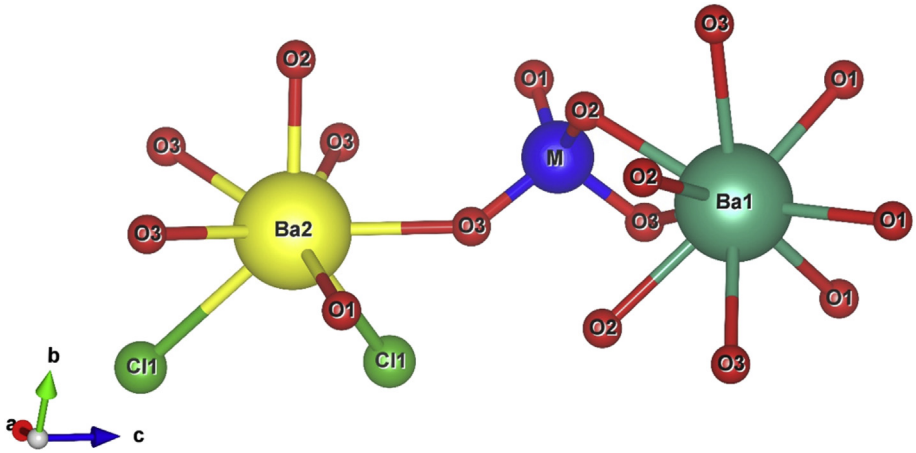

Fig. 5. A fragment of $Ba_5Mn_{3-x}V_xO_{12}Cl/Ba_5Mn_{3-x}P_xO_{12}Cl$ unit cell: big dark turquoise and yellow spheres represent different crystallographic positions of Ba^{2+} – 4f and 6h accordingly, blue spheres – M^{5+}, Cl^- – green spheres, O^{2-} – red spheres. (For interpretation of the references to color in this figure legend, the reader is referred to the web version of this article.)

wavenumbers (420 cm^{-1} to 290 cm^{-1}) pertain to stretching vibrations (ν_2– symmetrical and ν_4– asymmetrical). Mn–O and V–O bond distances are very similar and vibrational peaks of $(VO_4)^{3-}$ and $(MnO_4)^{3-}$ functional groups might be overlapped. $(PO_4)^{3-}$ group's deformation modes lie in the region with higher around 800 cm^{-1}.

3.4. Magnetic properties

Magnetic properties of the parent compound $Ba_5Mn_3O_{12}Cl$ were

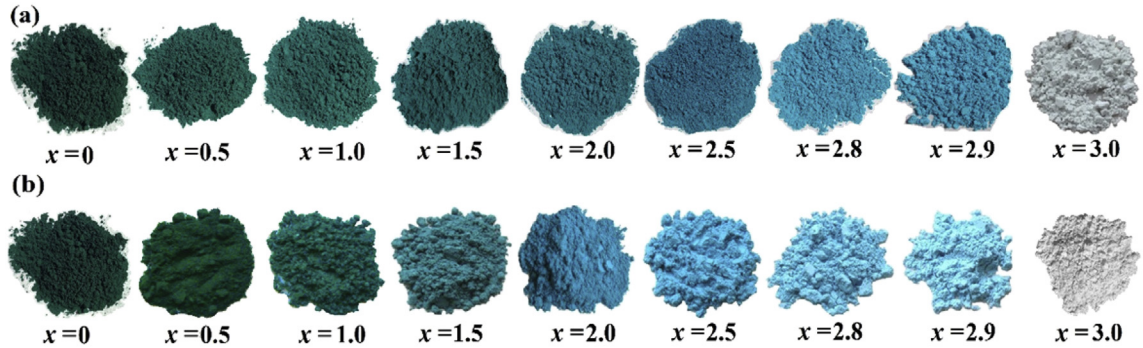

Fig. 6. Colors of $Ba_5Mn_{3-x}V_xO_{12}Cl$ (a) and $Ba_5Mn_{3-x}P_xO12Cl$ (b) samples. (For interpretation of the references to color in this figure legend, the reader is referred to the web version of this article.)

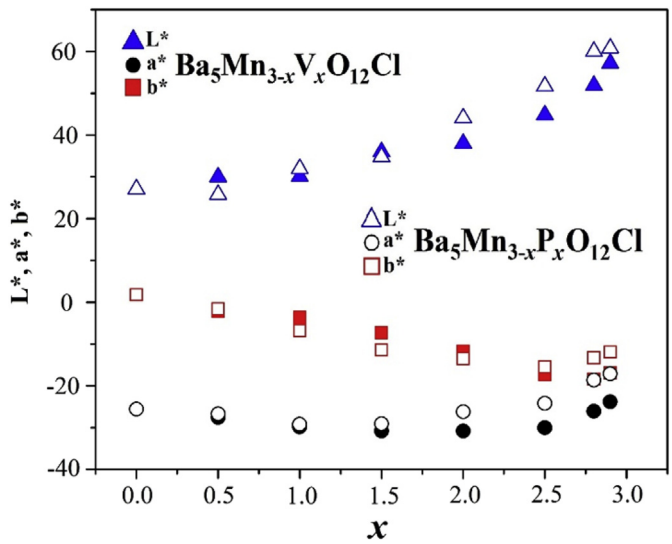

Fig. 7. L*(represent a black (L* = 0)/white (L* = 100) component of color), a* (responsible for a red (a*>0)/green (a*<0) component), b*(represent a yellow (b*>0)/blue (b*<0) components) parameters of samples as a function of *x*. (For interpretation of the references to color in this figure legend, the reader is referred to the web version of this article.)

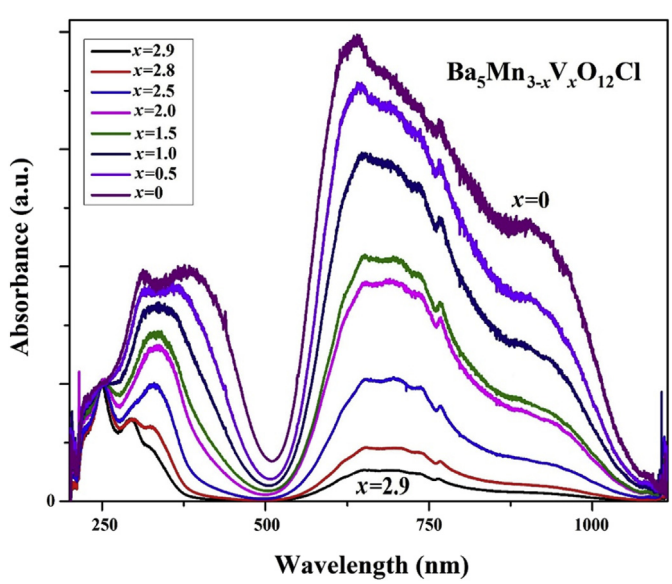

Fig. 8. Diffuse-reflectance spectra of the $Ba_5Mn_{3-x}V_xO_{12}Cl$ series.

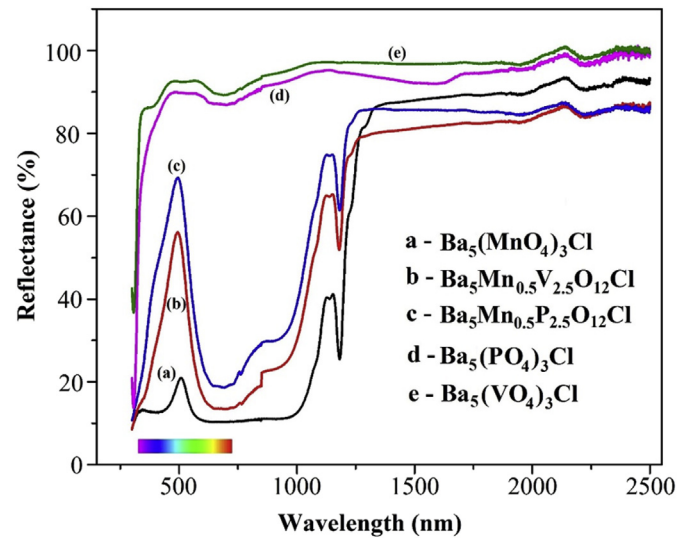

Fig. 9. UV–vis and NIR reflectance (%) of $Ba_5Mn_{3-x}V_xO_{12}Cl$ (x = 0, 2.5, 3) and $Ba_5Mn_{3-x}P_xO_{12}Cl$ (x = 0, 2.5, 3) samples as a function of wavelength (nm).

reported earlier [64]; however those of the solid solutions have not been studied systematically. We measured magnetic susceptibilities of three phases: $Ba_5Mn_3O_{12}Cl$, $Ba_5Mn_{1.5}V_{1.5}O_{12}Cl$ and $Ba_5Mn_{1.5}P_{1.5}O_{12}Cl$. Based on magnetic susceptibility vs. temperature and $1/\chi$ vs. temperature graphs (Fig. 10) all samples show paramagnetic behavior in the measured temperature region (5 K–300 K). Calculated magnetic moments are listed in Table 7; the calculated moments are in agreement with the theoretical magnetic moment of Mn^{5+} (μ_{th} = 2.83); this indicates that manganese in all samples shows an oxidation state of 5 + with two unpaired electrons. The Curie and Weiss constants were calculated from the slope and intercept of the linear region of $1/\chi$ versus temperature.

4. Conclusions

We have successfully synthesized two solid solutions $Ba_5Mn_{3-x}V_xO_{12}Cl$ (x = 0–3.0) and $Ba_5Mn_{3-x}P_xO_{12}Cl$ (x = 0–3.0). All samples show intense turquoise and green colors. All phases were characterized using X-ray diffraction, optical, magnetic and IR measurements; for four samples ($Ba_5(MnO_4)_3Cl$; $Ba_5Mn_{2.5}V_{0.5}O_{12}Cl$; $Ba_5Mn_{0.2}V_{2.8}O_{12}Cl$ and $Ba_5Mn_{0.5}P_{2.5}O_{12}Cl$) neutron data were collected and their structures were refined. The synthesized compounds show great potential as environmentally benign

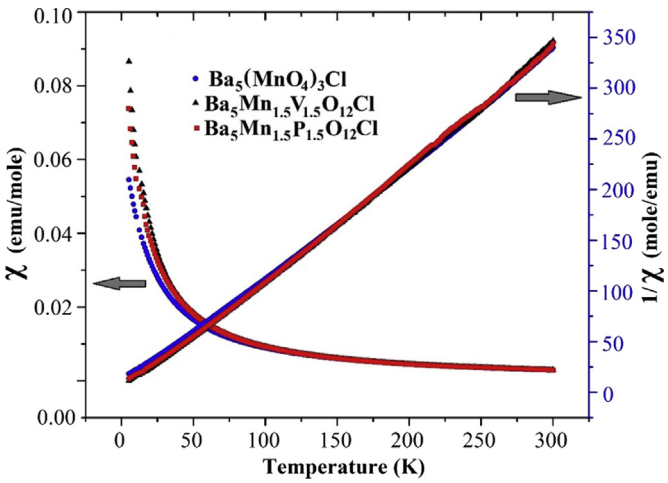

Fig. 10. Magnetic susceptibility and inverse magnetic susceptibility of $Ba_5(MnO_4)_3Cl$, $Ba_5Mn_{1.5}V_{1.5}O_{12}Cl$ and $Ba_5Mn_{1.5}P_{1.5}O_{12}Cl$; 1 emu (cgs units) = 10^{-3} A m^2 (SI units).

Table 7
Calculated magnetic moments, Curie and Weiss constants of $Ba_5(MnO_4)_3Cl$, $Ba_5Mn_{1.5}V_{1.5}O_{12}Cl$ and $Ba_5Mn_{1.5}P_{1.5}O_{12}Cl$ samples.

Compound	T region (K)	C	θ (K)	μ_{eff} (μ_B)
$Ba_5(MnO_4)_3Cl$	200–300	0.8424	14.92	2.61
$Ba_5Mn_{1.5}V_{1.5}O_{12}Cl$	200–300	0.8107	19.37	2.57
$Ba_5Mn_{1.5}P_{1.5}O_{12}Cl$	200–300	1.0314	−18.27	2.84

inorganic cool pigments.

Acknowledgments

This research was supported by National Science Foundation (DMR – 1508527). The identification of any commercial product or trade name does not imply endorsement or recommendation by the National Institute of Standards and Technology.

Appendix A. Supplementary data

Supplementary data related to this article can be found at http://dx.doi.org/10.1016/j.solidstatesciences.2015.12.001.

References

[1] A.E. Smith, H. Mizoguchi, K. Delaney, N.A. Spaldin, A.W. Sleight, M.A. Subramanian, Mn^{3+} in trigonal bipyramidal coordination: a new blue chromophore, J. Am. Chem. Soc. 131 (2009) 17084–17086.
[2] P. Jiang, J. Li, A. Ozarowski, A.W. Sleight, M.A. Subramanian, Intense turquoise and green colors in brownmillerite-type oxides based on Mn^{5+} in $Ba_2In_{2-x}Mn_xO_{5+x}$, Inorg. Chem. 52 (2013) 1349–1357.
[3] J.C. Elliott, R.M. Wilson, S.E.P. Dowker, Apatite structures, Adv. X-ray Analysis 45 (2002) 172–181.
[4] A.V. Knyazev, N.G. Chernorukov, E.N. Bulanov, Apatite-structured compounds: synthesis and high-temperature investigation, Mater. Chem. Phys. 132 (2012) 773–781.
[5] P. Wu, Y.Z. Zeng, C.M. Wang, Prediction of apatite lattice constants from their constituent elemental radii and artificial intelligence methods, Biomaterials 25 (2004) 1123–1130.
[6] W.E. Baker, An X-ray diffraction study of synthetic members of the pyromorphite series, Am. Mineral. 51 (1966) 1712–1721.
[7] N.G. Chernorukov, A.V. Knyazev, E.N. Bulanov, Phase transitions and thermal expansion of apatite-structured compounds, Inorg. Mater. 47 (2) (2011) 172–177.
[8] P.G. Cooray, A carbonate-bearing fluor-chlor-hydroxyapatite from Matale, Ceylon, Am. Mineral. 55 (1970) 2038–2041.
[9] C. Guillemin, J. Prouvist, M. Wintenberger, Different fibrous mimetite (prixite) and vanadinite, Bull. Soc. Franc. Min. Crist. LXXVIII (1955) 301–306 (in French).
[10] F. Laufec, Romanskala, J. Haloda, I. Cisarova, Crystal structure of vanadinite: refinement of anisotropic displacement parameters, J. Czech Geol. Soc. 51 (3–4) (2006) 271–275.
[11] V.L. Merker, H. Wondratshek, Lead compounds with apatite structures, especially lead iodo- and lead bromo-apatite, Z. Anorg. Allg. Chem. 300 (1959) 41–50 (in German).
[12] J.S.R.K. Rao, R.D. Raju, Apatite-structurally intermediate between flour-apatite and dahlliate from Koduru, A.P, J. Indian Geo. Assoc. 13 (1971) 79–81.
[13] G. Buvaneswari, U.V. Varadaraju, Synthesis and characterization of new apatite-related phosphates, J. Solid Stata Chem. 149 (2000) 133–136.
[14] A.V. Knyazev, E.N. Bulanov, A.O. Korshunov, O.V. Krasheninnikova, Synthesis and thermal expansion of some lanthanide-containing apatites, Inorg. Mater. 49 (11) (2013) 1133–1137.
[15] M. Pasero, A.R. Kampf, C. Ferraris, I. Pekov, et al., Nomenclature of the apatite supergroup minerals, Eur. J. Mineral. 22 (2010) 163–179.
[16] A.V. Knyazev, M. Maczka, E.N. Bulanov, M. Ptak, S.S. Belopolskaya, High-temperature thermal and X-ray diffraction studies, and room-temperature spectroscopic investigation of some inorganic pigments, Dyes Pigments 91 (2011) 286–293.
[17] P.D. Johnson, J.S. Prener, J.D. Kingsley, Apatite: origin of blue color, Science 141 (1963) 1179–1180.
[18] A.V. Knyazev, N.G. Chernorukov, E.N. Bulanov, High-temperature investigation of $Ba_5(A^VO_4)_3Cl$ (A^V=P, V, Mn), Vestnik Lobachevsky State Univ. Nizhni Novgorod 6 (2010) 82–87 (in Russian).
[19] D.A. Grisafe, F.A. Hummel, Pentavalent ion substitutions in the apatite structure Part B. color, J. Solid Sate Chem. 2 (1970) 167–175.
[20] K. Dardenne, D. Vivien, D. Huguenin, Color of Mn(V)-substituted apatites $A10((B,Mn)O_4)_6F_2$, A=Ba, Sr, Ca; B=P, V, J. Solid State Chem. 146 (1999) 464–472.
[21] L. Brixner, J.F. Weiher, A magnetic study of a chlorapatite of manganese, $Ba_5(MnO_4)_3Cl$, Inorg. Chem. 7 (1968) 1474–1475.
[22] D. Reinen, H. Lachwa, R. Allmann, Colour and constitution for Mn^V in tetrahedral oxygen coordination. I. An EPR and ligand field spectroscopic investigation of Mn^V in apatite phases and the structure of $Ba_5(MnO_4)_3Cl$, Z, Anorg. Allg. Chem. 542 (1986) 71–88 (in German).
[23] D.A. Fielder, J.H. Albering, J.O. Besenhard, Characterization of strontium and barium manganates by abrasive stripping voltammetry, J. Solid State Electrochem. 2 (1998) 413–419.
[24] T.J. White, Z.L. Dong, Structural derivation and crystal chemistry of apatites, Acta Crystallogr. Sect. B 59 (2003) 1–16.
[25] Y.H. Roh, S.T. Hong, Apatite-type $Ba_5(VO_4)_3Cl$, Acta Crystallogr. 61 (2005) i140–i142.
[26] Z. Xia, Y. Liang, W. Huang, et al., Molten salt synthesis and photoluminescence properties of novel red emitting phosphores $Ba_5(VO_4)_3Cl$: Eu^{3+}, K^+, J. Mater. Sci. Mater. Electron 24 (2013) 5111–5116.
[27] A.V. Kruzhalov, F.F. Gavrilov, N.I. Kordyukov, et al., Luminescence of alkaline earth chlorovanadates, Zhurnal Prikl. Spectroskopii 21 (1974) 631–635 (in Russian).
[28] H.P. Beck, M. Douiheche, R. Haberkorn, H. Kohlmann, Synthesis and characterisation of chloro-vanadato-apatites $M_5(VO_4)_3Cl$ (M=Ca, Sr, Ba), Solid State Sci. 8 (2006) 64–70.
[29] M. Hata, F. Marumo, S. Iwai, H. Aoki, Structure of barium chlorapatite, Acta Crystallogr. Sect. B 35 (1979) 2382–2384.
[30] C. Li, Y. Li, X. Wang, Study on the effect of apatite structure on spectroscopic properties of bismuth activated alkaline earth metal chlorophosphate [$M_5(PO_4)_3Cl$; M=Ca, Sr and Ba], Mater. Chem. Phys. 139 (2013) 220–224.
[31] G. Ju, Y. Hu, C. Li, X. Wang, Persistent luminescence and its mechanism of $Ba_5(PO_4)_3Cl$: Ce^{3+}, Eu^{2+}, J. Appl. Phys. 3 (2012), 113508–113508.
[32] H.S. Yoo, S. Vaidyanathan, S.W. Kim, D.Y. Jeon, Synthesis and photoluminescence properties of Yb^{2+} doped $Ba_5(PO_4)_3Cl$ phosphor for white light-emitting diodes, Opt. Mater. 31 (2009) 1555–1558.
[33] J. Xiao-Long, Preparation and luminescence properties of $Ba_5(PO_4)_3Cl$: Eu^{2+} phosphor, Chin. J. Luminescence 4 (2014) 409–412 (in Chinese).
[34] S.J. Yue, D. Pe, B. Cui, Xue, et al., Photoluminescence and energy transfer of Ce^{3+} and Tb^{3+} co-doped $Ba_5(PO_4)_3Cl$ phosphor for light-emitting diodes, Appl. Mech. Mater. 401 (2013) 796–799.
[35] J. Guifang, Y. Hu, C. Li, et al., Persistent luminescence in $Ba_5(PO_4)_3Cl$: Eu^{2+}, R^{3+} (R=Y, La, Ce, Gd, Tb and Lu), Mater. Res. Bull. 48 (2013) 2598–2603.
[36] G. Ju, Y. Hu, L. Chen, X. Wang, Photochromism of rare earth doped barium haloapatite, J. Photochem. Photobiol. A Chem. 251 (2013) 100–105.
[37] M.A. Noginov, G.B. Loutts, C.E. Bonner, et al., Crystal growth and characterization of a new laser material, Nd:$Ba_5(PO_4)_3Cl$, JOSA B 17 (2000) 1329–1334.
[38] M. Sato, T. Tanaka, M. Ohta, Photostimulated luminescence and structural characterization of $Ba_5(PO_4)_3Cl$:Eu^{2+} phosphors, J. Electrochem. Soc. 141 (1994) 1851–1855.
[39] M. Herren, H.U. Gudel, High-resolution near-infrared luminescence of manganese (V) in tetrahedral oxo coordination, Chem. Phys. Lett. 183 (2001) 98–102.
[40] K. Forster, M. Greenblatt, J. Pifer, Electron spin resonance of CrO_4^{3-} in barium chloroapatite, $Ba_5(PO_4)_3Cl$, J. Solid State Chem. 30 (1979) 121–124.
[41] L. Suchow, Studies of color centers produced in apatite halophosphates by shortwave ultraviolet radiation, J. Electrochem. Soc. 108 (1961) 847–851.
[42] M. Shang, D. Geng, D. Yang, X. Kang, Y. Zhang, J. Lin, Luminescence and energy transfer properties of $Ca_2Ba_3(PO_4)_3Cl$ and $Ca_2Ba_3(PO_4)_3Cl$:A (A = Eu^{2+}/Ce^{3+}/Dy^{3+}/Tb^{3+}) under UV and low-voltage electron beam excitation, Inorg. Chem.

52 (2013) 3102–3112.
[43] G. Bai, M.K. Tsang, J. Hao, Tuning the luminescence of phosphors: beyond conventional chemical method, Adv. Opt. Mater 3 (2015) 431–462.
[44] http://en.wikipedia.org/wiki/Turquoise (accessed September 2015()).
[45] G.N. Kukushkina, A.N. Demidovskaya, O.T. Irklievskaya, V.N. Mokhort, T.I. Kurlovich, L.N. Stepanova, N.M. Gizun, Ceramic blue-green pigment, U.S.S.R. Patent No. 1273338 (30 November 1986).
[46] G.N. Kukushkina, A.N. Demidovskaya, O.T. Irklievskaya, V.N. Mokhort, T.I. Kurlovich, L.N. Stepanova, V.L. Petrusev, Ceramic turquoise pigment, U.S.S.R. Patent No. 1281534 (7 January 1987).
[47] I.V. Pishch, K.E. Biryukova, L.V. Slepukhova, Ceramic turquoise pigment containing Cr2O3, ZnO, Al2O3, Co2O3 and B2O3, U.S.S.R. Patent No. 1065358 (7 January 1984).
[48] A.C. Larson, R.B. Von Dreele, General structure analysis system (GSAS), Los Alamos Natl. Lab. Rep. LAUR (2014) 86–784.
[49] EXPGUI, a graphical user interface for GSAS: B.H. Toby, J. Appl. Crystallogr. 34 (2001) 210.
[50] C. Hormillosa, S. Healy, T. Stephen, I.D. Brown, Bond Valence Calculator, Version 2.0, 1993. http://www.ccp14.ac.uk (accesses July 2015).
[51] M.E. Sherif, O.A. Bayoumi, T.Z.N. Sokkar, Prediction of absorbance from reflectance for an absorbing-scattering fabric, Color Res. Appl. 22 (1997) 32.
[52] G.A. Bain, J.F. Berry, Diamagnetic corrections and Pascal's constants, J. Chem. Educ. 85 (2008) 532–536.
[53] R.D. Shannon, Revised effective ionic radii and systematic studies of interatomic distances in halides and chalcogenides, Acta Crystallogr. Sect. A 32 (1976) 751–767.
[54] K. Robinson, G.V. Gibbs, P.H. Ribbe, Quadratic elongation: a quantitative measure of distortion in coordination polyhedra, Science 172 (1971) 567–570.
[55] M.E. Fleet, Distortion parameters for coordination polyhedra, Mineral. Mag. 40 (1976) 531–533.
[56] J. Schanda, Colorimetry, first ed., Understanding the CIE System, Wiley-Intersience, 2007.
[57] J.D. Kingsley, J.S. Prener, B. Segall, Spectroscopy of MnO_4^{3-} in calcium halophosphates, APS 137 (1965) 189.
[58] R. Borromei, L. Oleari, P. Day, Electronic spectrum of the manganate (V) ion in different host lattices, J. Chem. Soc. 77 (1981) 1563–1578.
[59] M.A. Scott, B. Henerson, H.G. Gallaghen, T.P.J. Han, Optical spectroscopy of $(MnO_4)^{3-}$ and $(VO_4)^{3-}$ in $Sr_{10}(VO_4)_6F_2$, J. Phys. Condens. Matter 9 (1997) 9893–9908.
[60] K. Dardenne, D. Vivien, F. Ribot, et al., Mn(V) polyhedron size in $Ba_{10}((P,Mn))O_4)_6F_2$: vibrational spectroscopy and EXAFS study, Eur. J. Solid State Inorg. Chem. 35 (1998) 419–431.
[61] A.V. Knyazev, E.N. Bulanov, A.N. Lapshin, Synthesis, Spectroscopic Study and Factor Group Analysis of Chloride Trisvanadates of Divalent Cations $M^{II}_5(VO_4)_3Cl$ (M^{II}=Ca, Sr, Ba, Cd, Pb), Vestnik of Lobachevsky State University of Nizhni Novgorod 3, 2012, pp. 87–91 (in Russian).
[62] K. Nakamoto, IR and Raman Spectra of Inorganic and Coordination Compounds (Mir, Moscow, 1991, p. 121 (in Russian).
[63] C. Boechat, J.-G. Eon, A. Rossi, et al., Structure of vanadate in calcium phosphate and vanadate apatite solid solutions, J. Phys. Chem. A 2 (2000) 4225–4230.
[64] L.H. Brixner, J.F. Weiher, A magnetic study of a chlorapatite of manganese, $Ba_5(MnO_4)_3Cl$, Inorg. Chem. 7 (1968) 1474–1475.